ADVANCING EARTH AND SPACE SCIENCE

Geochemistry, Geophysics, Geosystems

RESEARCH ARTICLE
10.1029/2020GC008972

Key Points:
- We use seismic and thermochronological data to determine the thermal structure of the crust in the central Southern Alps
- Exhumation rates of 8±3 mm/yr are localized near Aoraki/Mount Cook, with peak exhumation rates elsewhere of 1–2 mm/yr
- High modeled BDT zone temperatures of 410–430°C may reflect the effects of elevated fluid pressures and/or high strain rates

Supporting Information:
- Supporting Information S1

Correspondence to:
K. Michailos,
konstantinos.michailos@unil.ch

Citation:
Michailos, K., Sutherland, R., Townend, J., & Savage, M. K. (2020). Crustal thermal structure and exhumation rates in the Southern Alps near the central Alpine Fault, New Zealand. *Geochemistry, Geophysics, Geosystems*, *21*, e2020GC008972. https://doi.org/10.1029/2020GC008972

Received 12 FEB 2020
Accepted 19 JUN 2020
Accepted article online 10 JUL 2020

Crustal Thermal Structure and Exhumation Rates in the Southern Alps Near the Central Alpine Fault, New Zealand

Konstantinos Michailos[1,2], Rupert Sutherland[1], John Townend[1], and Martha K. Savage[1]

[1]School of Geography, Environment and Earth Sciences, Victoria University of Wellington, Wellington, New Zealand, [2]Now at Institute of Earth Sciences, University of Lausanne, Lausanne, Switzerland

Abstract We investigate orogenic uplift rates and the thermal structure of the crust in the hanging wall of the Alpine Fault, New Zealand, using the hypocenters of 7,719 earthquakes that occurred in the central Southern Alps between late 2008 and early 2017, and previously published thermochronological data. We assume that the base of the seismogenic zone corresponds to a brittle-ductile transition at some fixed temperature, which we estimate by fitting the combined thermochronological data and distribution of seismicity using a multi-1-D approach. We find that exhumation rates vary from 1 to 8 mm/yr, with maximum values observed in the area of highest topography near Aoraki/Mount Cook, a finding consistent with previous geologic and geodetic analyses. We estimate the temperature of the brittle-ductile transition beneath the Southern Alps to be 410–430°C, which is higher than expected for Alpine Fault rocks whose bulk lithology is likely dominated by quartz. The high estimated temperatures at the base of the seismogenic zone likely reflect the unmodeled effects of high fluid pressures or strain rates.

Plain Language Summary The Southern Alps of New Zealand have formed during the last 10 million years as a result of collision between the Pacific and Australian plates. The Alps are bounded to the northwest by the Alpine Fault, which produces earthquakes of magnitude ~8 every 300 years. Using observations of 7,700 much smaller earthquakes that occurred between 2008 and 2017, and 150 thermochronological measurements, which give the times at which different minerals cooled below specific temperatures, we have constructed a thermal model of the Southern Alps that enables us to estimate the rates at which the Alps are being uplifted and hence to estimate the temperature at the source locations of earthquakes. The pattern of uplift we determine is consistent with previous geological and geodetic results and enables us to calculate the temperature at which each earthquake occurred. The base of earthquake activity is at 410–430°C, which is hotter than anticipated. We suggest that high fluid pressures or strain rates cause the Southern Alps to deform at higher temperatures than would otherwise be the case. The shallowing of seismicity near Aoraki/Mount Cook, where we estimate rapid uplift and erosion at 8±3 mm/yr, is conspicuous, though we also estimate high temperatures for earthquakes elsewhere in the Southern Alps, where uplift rates are inferred to be 1–2 mm/yr.

1. Introduction

We use the distribution of crustal earthquakes' hypocentral depths and thermochronological data as constraints on models of the thermal structure of the crust in a young transpressive orogen, the central section of the Southern Alps, South Island, New Zealand. Ongoing interaction between the Australian and Pacific plates has formed the Southern Alps orogen (Walcott, 1998), bounded to the northwest by the Alpine Fault, an active plate-bounding oblique strike-slip fault of ~800 km length (Wellman & Willet, 1942) that has accommodated at least 450 km of dextral offset since 25 Ma (Sutherland, 1999). Seismic reflections beneath the central Southern Alps reveal an eastward-dipping Alpine Fault with a dip of 40–50°, flattening in the lower crust (~35 km depth) and forming a décollement (Davey et al., 1995; Stern et al., 2001, 2007). The Southern Alps orogen is structurally and kinematically asymmetric, exhibiting high rates of uplift, exhumation, rainfall, and erosion between the Alpine Fault and the Main Divide (Koons et al., 2003). The orientation and rate of the plate motion are 245 ± 1° and 39.5 ± 0.7 mm/yr (DeMets et al., 2010). This makes the plate motion oblique to the surface orientation of the central section of the Alpine Fault (~055°), resulting in relative velocities of 39 mm/yr parallel and 7 mm/yr perpendicular to the fault (Beavan et al., 1999; Norris & Cooper, 2001). The Alpine Fault accommodates 27±5 mm/yr of the strike-slip component of plate motion (Norris & Cooper, 2001). The convergent component of plate motion is responsible for crustal thickening and exhumation of crustal rocks taking place in the hanging wall of the Alpine Fault (Norris & Cooper, 2007; Walcott, 1998). This convergence is thought to have begun between 10 and 5 Ma (Sutherland, 1995; Walcott, 1998) or as early as 20–14 Ma (Cande & Stock, 2004; Ring et al., 2019).

Geological (Herman et al., 2007, 2009; Kamp et al., 1989; Little et al., 2005; Norris & Cooper, 2001; Wellman, 1979) and geodetic studies (Beavan et al., 2004, 2010) have long established that the most rapid exhumation of the Alpine Fault's Pacific plate hanging wall takes place in the central Southern Alps, governing both the mechanical behavior and the thermal structure of the orogen (Koons et al., 2003). Wellman (1979) first determined uplift rates in the central Southern Alps of as much as 10 mm/yr, using Quaternary slip rate measurements. Fission track dating (Kamp et al., 1989; Tippett & Kamp, 1993) later found there to be a relationship between the zonations of young cooling ages and rapid exhumation rates in the Southern Alps. Little et al. (2005) mapped contours of fission-track, Ar/Ar, and K-Ar ages in several different mineral systems to estimate uplift rates near the central Alpine Fault and obtained rates of ∼6–9 mm/yr near Fox and Franz Josef Glaciers. Beavan et al. (2010) calculated the relative vertical component of velocity across the Southern Alps using 10 years of continuous and semi-continuous global positioning system (GPS) data and determined a peak uplift rate of ∼5 mm/yr near the Main Divide on a transect across the Southern Alps (Beavan et al., 2004).

In contrast to the detailed observations and models of uplift that have been made, knowledge of the thermal structure of the central Southern Alps is somewhat limited, although important in providing insights into rock rheology and the kinematics of faulting. One of the first models of the thermal structure of the Southern Alps was developed by Koons (1987), who treated the Alpine Fault as a vertical discontinuity, and assumed uplift rates of approximately 10 mm/yr east of the fault, a 4 Myr age for the duration of the exhumation of the Southern Alps, and purely conductive heat transfer. This model suggested that a zone of rapid uplift and thermally weakened strength adjacent to the Alpine Fault, manifest as high horizontal strain rates. More recent studies (e.g., Allis & Shi, 1995; Cross et al., 2015; Kidder et al., 2018; Shi et al., 1996; Sutherland et al., 2012, 2017; Toy et al., 2010) have all indicated the presence of high temperatures at shallow depths (∼8 km) near the Alpine Fault, particularly in a narrow zone of 10–25 km width immediately southeast of the fault's surface trace. A clear manifestation of these high subsurface temperatures is the existence of hot springs in the area (e.g., Allis et al., 1979; Cox et al., 2015).

Numerous studies worldwide have examined the relationship between the distribution of earthquakes' hypocentral depths and parameters controlling the crustal strength distribution, including heat flow, lithology, total crustal strength, rheology, and mechanics (e.g., Albaric et al., 2009; Bonner et al., 2003; Doser & Kanamori, 1986; Hauksson & Meier, 2018; Zoback et al., 2002). The deformation of crustal rocks in response to imposed stresses varies with depth under different temperature and pressure conditions (Chen & Molnar, 1983; Sibson, 1984; Scholz, 2002). According to prevailing models (e.g., Scholz, 1988; Sibson, 1983), differential stress increases linearly with depth in the upper brittle portion of the crust and reaches a peak in the brittle-ductile transition (BDT) zone, below which it decreases approximately exponentially. Many factors including temperature, strain rate, pore fluid pressure, lithology, water content, fault geometry, and stress regime (Scholz, 1998; Sibson, 1984; Zoback & Townend, 2001) affect the depth of the BDT zone, which roughly corresponds to the maximum depths of low- and moderate-magnitude seismicity (Chen & Molnar, 1983; Scholz, 1988; Sibson, 1982, 1984) and the depth to which rupture extends in large earthquakes (Jackson, 2002; Magistrale & Zhou, 1996; Sibson, 1982, 1984). Recent studies however have suggested that large earthquakes sometimes or always also rupture the deeper creeping section of the fault zone (Beeler et al., 2018; Jiang & Lapusta, 2016; Shaw & Wesnousky, 2008).

The lower cutoff depth of the seismogenic zone adjacent to the central Alpine Fault has previously been estimated to be 8–14 km using hypocentral earthquake depths (Boese et al., 2012; Bourguignon et al., 2015; Leitner & Eberhart-Phillips, 2001). Recent work by Michailos et al. (2019) revealed systematic changes in the seismicity cutoff depths along the strike of the Alpine Fault and showed that these cutoff depths agree well with geodetically inferred locking depths (Beavan et al., 2007; Lamb & Smith, 2013; Wallace et al., 2007). Here, we model the distribution of exhumation rates (i.e., the rate of rock motion relative to the

10.1029/2020GC008972

topographic surface) and the thermal structure of the crust in the Southern Alps to explain seismological and thermochronological observations.

2. Data and Methods

2.1. Seismicity Data

We analyze the distribution of 7,719 hypocentral depths from the relocated microseismicity catalog of Michailos et al. (2019) that spans the central section of the Alpine Fault for the period between late 2008 and early 2017 (Figure 1a). This catalog was created by combining raw seismic waveform data from five different temporary deployments and five permanent ("GeoNet") seismometers. It includes the largest number of high-precision earthquake locations obtained to date for the central Southern Alps region, with location uncertainties generally less than 0.5 km in both the horizontal and vertical directions. The GeoNet catalog in the same area and for the same period contains 2,151 events of mostly default depths (Figure 2). We include all the relocated earthquake locations and do not perform any declustering as we have not observed any major aftershock sequences. Seismicity during the 8 years analyzed mainly occurred in swarms of low-magnitude earthquakes (Boese et al., 2012, 2014; Michailos et al., 2019).

2.1.1. Earthquake Hypocenter Analysis

To represent the spatial distribution of seismicity, we first divide the study area into subregions using a recursive quadtree clustering algorithm following the method described by Townend and Zoback (2001, 2004). The subregions obtained with this method form a mesh of square bins that are smaller in areas of higher earthquake density (Figure S1 of the supporting information). This enables us to take into consideration lateral variations in hypocentral depths.

We use cumulative distribution functions of hypocentral depths for the earthquakes (Figures S2 and S3 of the supporting information) to calculate the upper and lower limits of seismicity in each bin. A linear regression curve is fit to the cumulative distribution function in each bin between the 10% and 90% limits (Figure 3). We exclude the upper and lower portions of the cumulative distributions for two reasons. First, earthquake locations in the top (shallow) limits of these distributions are typically poorly determined. Second, the bottom (deep) limit of these distributions is likely controlled in part by unmodeled processes operating below the BDT (i.e., in the deeper ductile part of the crust) that are of secondary interest here (Figure 3a).

By extrapolating the fitted linear regression curves, we estimate values for the lower seismicity cutoff depth (z_0; 0%) and the upper seismicity cutoff depth (z_{100}; 100%) and their standard errors. Figure 3 shows four contrasting hypocentral distributions with their corresponding linear regression curves and the upper and lower seismicity cutoff depth estimates. We exclude bins that contain fewer than 30 observations, which are mainly located on the periphery of the seismic network, because their cutoff depth estimates have larger uncertainties (e.g., bin 74; Figure 3d). Details for the rest of the 45 bins can be found in Figures S4 and S5 of the supporting information.

2.2. Thermochronological Data

Thermochronological data provide measurements of the times and rates at which rocks have cooled as they moved towards the surface during exhumation (Dodson, 1973). The age estimates are based on the naturally occurring radioactive decay or spontaneous fission of a parent nuclide and the accumulation of a corresponding daughter product (e.g., U-Th/He dating) or crystal damage (e.g., fission-track; Peyton & Carrapa, 2013).

Each thermochronological system is reset at high temperatures or depths, under which conditions daughter products do not accumulate. For example, He atoms are not retained (U-Th/He dating), and fission tracks are healed (annealed). With decreasing temperature and depth, the rock reaches a specific range of temperatures within which a proportion of daughter products are retained in the system (Reiners & Brandon, 2006). These temperature ranges are called the partial retention zones (PRZs; U-Th/He) or partial annealing zones (PAZs; fission-track). The annealing process for crystal damage occurs over a range of temperatures for different thermochronometers (e.g., apatite fission-track, AFT, 80–110°C; zircon fission-track, ZFT, 190–230°C, zircon (U-Th)/He, ZHe, 140–180°C, and apatite (U-Th)/He, AHe, 40–70°C; Gleadow & Duddy, 1981; Reiners et al., 2004; Tagami, 2005). Using the RPZ and PAZ information (i.e., each thermochronometer's closure over a given temperature range) and assuming a constant cooling rate, we can compute a single temperature on

10.1029/2020GC008972

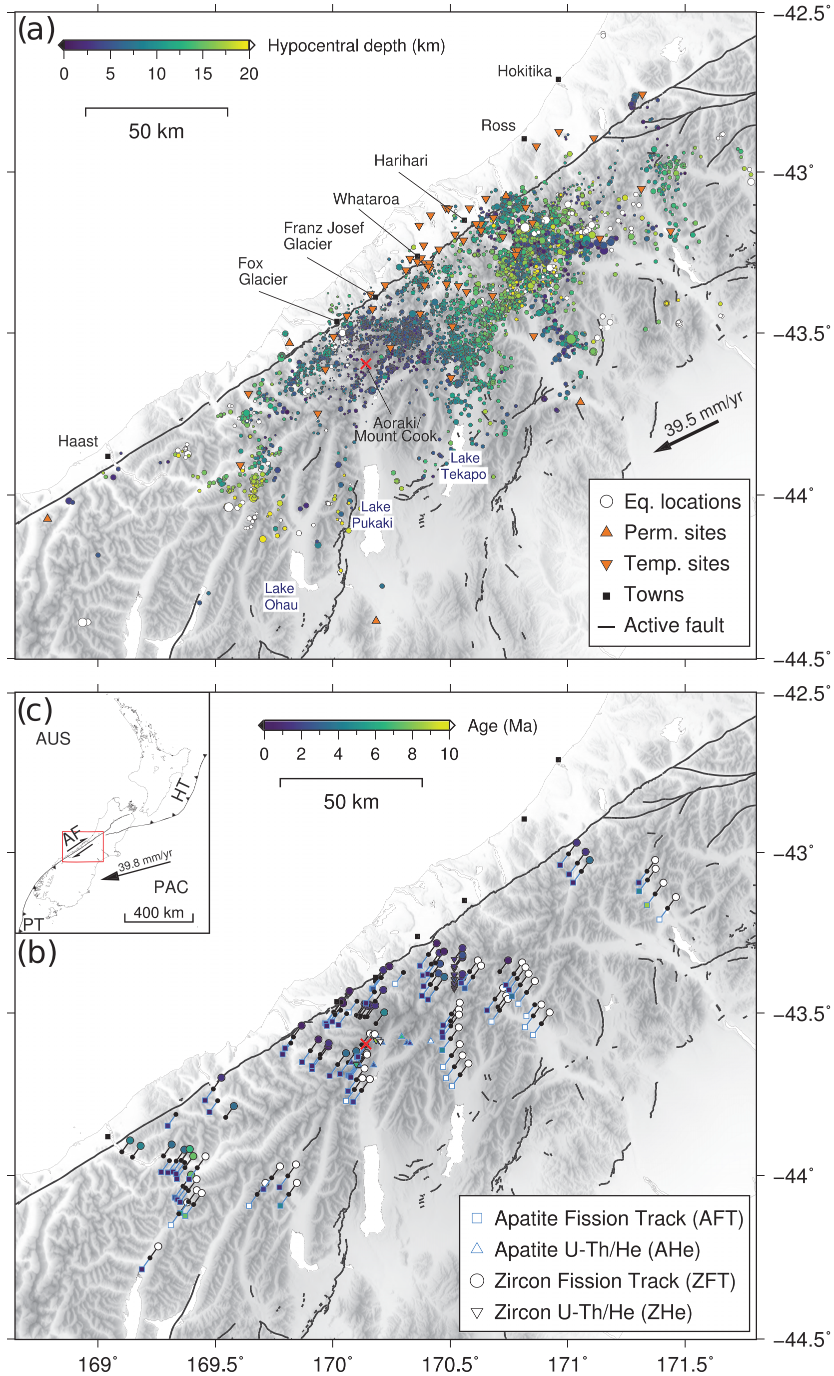

Figure 1. (a) Map of the central Southern Alps region showing the epicenters of 7,719 earthquakes that occurred between November 2008 and March 2017 (Michailos et al., 2019). Circle sizes are scaled according to their respective magnitudes and colored according to depth. Temporary and permanent (GeoNet) seismic sites are shown by orange inverted triangles and orange triangles, respectively. Aoraki/Mount Cook is represented by a red cross. Black lines show active faults from the New Zealand Active Faults Database (http://data.gns.cri.nz/af/). The arrow indicates the local velocity of the Pacific Plate relative to Australia (~39.5 mm/yr; DeMets et al., 2010). (b) Spatial distribution of the 194 thermochronological data near the central Alpine Fault used in this study colored according to their ages (Batt & Braun, 1999; Batt et al., 2000; Herman et al., 2007, 2009; Kamp et al., 1989; Ring & Bernet, 2010; Seward, 1989; Tippett & Kamp, 1993). Apatite fission-track (AFT) and apatite U-Th/He (AHe) ages are shown by squares and triangles with blue edges, respectively. Zircon fission-track (ZFT) and zircon U-Th/He (ZHe) ages are depicted by circles and inverted triangles with black edges, respectively. (c) Inset map shows the location of the study area within New Zealand. PAC, Pacific Plate; AUS, Australian Plate; PT, Puysegur Trench; HT, Hikurangi Trough; and AF, Alpine Fault.

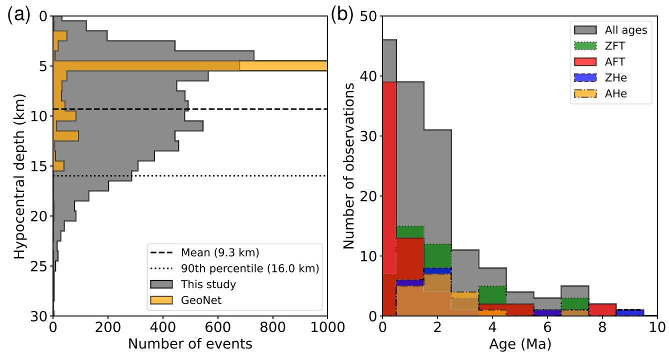

Figure 2. (a) Histogram of earthquake hypocentral depths for the relocated central Southern Alps microseismicity catalog (2008–2017) of Michailos et al. (2019) analyzed in this study (grey). The earthquake depth distribution histogram for the GeoNet catalog for the same area and period is shown for comparison (orange). The majority of GeoNet earthquake locations shown here have default hypocentral depths because of the sparser network spacing. (b) Histogram of apatite fission-track (AFT), zircon fission-track (ZFT), zircon U-Th/He (ZHe), and apatite U-Th/He (AHe) thermochronological ages (<10 Ma) near the central Alpine Fault (Batt & Braun, 1999; Batt et al., 2000; Herman et al., 2007, 2009; Kamp et al., 1989; Ring & Bernet, 2010; Seward, 1989; Tippett & Kamp, 1993).

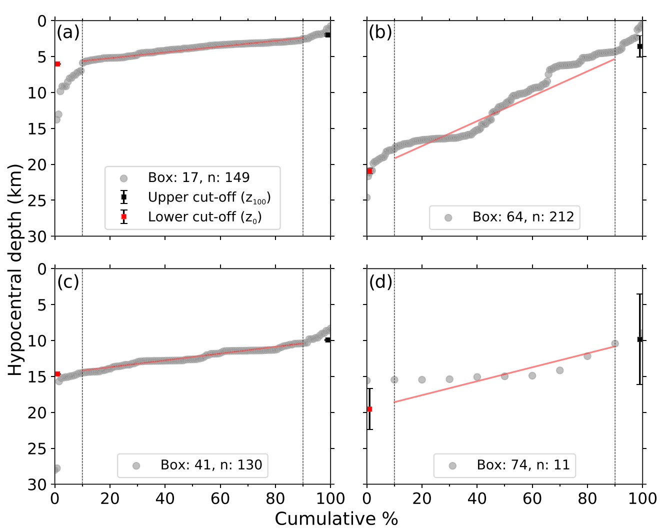

Figure 3. Illustrative examples of the cumulative distribution functions of hypocentral depths within bins 17, 41, 64, and 74; see Figure S1 of the supporting information for the locations of these bins. Red lines show linear regression curves fit within the 10–90% interval of the cumulative distribution functions, bounded by the black dashed lines. Red and black squares show the extrapolated lower (0%) and the upper seismicity cut-off depths (100%), respectively, obtained from the regression parameters. Vertical bars depict the 1σ error of the linear regression models. Panel (d) highlights the large uncertainties in the cutoff estimates for a box with too few observations.

the cooling path known as the effective closure temperature, T_c (Dodson, 1973; Reiners & Brandon, 2006). Moreover, by considering multiple thermochronometric systems with different closure temperatures together, detailed time-temperature paths can be constructed for individual samples and converted into exhumation rates. Table 1 summarizes the closure temperatures as a function of cooling rate for different thermochronometers (Reiners & Brandon, 2006).

We use a total of 194 thermochronological AFT, ZFT, ZHe, and AHe age estimates available across the central Southern Alps (Figure 1; Batt & Braun, 1999; Batt et al., 2000; Herman et al., 2007, 2009; Kamp et al., 1989; Ring & Bernet, 2010; Seward, 1989; Tippett & Kamp, 1993). Thermochronological ages increase with distance from the surface trace of the Alpine Fault (Herman et al., 2009; Warren-Smith et al., 2016). This trend has been previously interpreted to reflect the differential uplift and exhumation rates along the length of the Southern Alps orogen (Herman et al., 2007; Kamp et al., 1989; Tippett & Kamp, 1993). The available thermochronological data have ages of as much as 100 Myr (Figure 1). The central section of the Southern Alps close to the Alpine Fault is considered to be in a topographic steady state (i.e., undergoing approximately the same amount of uplift and erosion; Adams, 1981). This, however, is likely to have changed markedly with time. Recent work by Ring et al. (2019) suggests a two-phase history for exhumation during the last 14–10 Ma (~4 km/Myr until 2 Ma and ~6 km/Myr since then). Here we assume that the orogen has been in this state since 10 Ma, corresponding to the onset of convergence on the Alpine Fault (Sutherland, 1995; Walcott, 1998). Accordingly, we only use the thermochronological data with ages younger than 10 Ma (150 of 194 observations; Figure 2).

Published thermochronological age uncertainties represent only the analytical measurement errors. To include the spatial variability of thermochronological ages, we calculate the standard deviation of the nearest ages (≤10 km separations) and include this in the calculation of the total uncertainty (σ_{total}) as shown in the following equation:

$$\sigma_{total} = \sqrt{s^2 + \sigma^2} \quad (1)$$

Here s is the standard deviation of all ages that have a distance less than 10 km from a given thermochronological observation, and σ is the measurement error of the observation itself.

2.3. One-Dimensional Thermal Modeling

To construct an analytical model of crustal thermal structure as a function of uplift rate, we first assume 1-D steady-state exhumation. The depth to the base of the exhuming block is assumed constant and referred to here as the décollement depth (Z_{BASE}). The material moves through the block at a constant rate such that the inward flux at the bottom equals the outward flux at the top. The base and top of the block are assumed to have constant temperatures of T_{BASE} and T_0, respectively. We assume a constant temperature of $T_0 = 13°$ C at the upper boundary (Z_0; sea level) and do not address variations in temperature caused by groundwater advection (Cox et al., 2015; Sutherland et al., 2017), as discussed by Sutherland et al. (2009), Upton and Sutherland (2014), and Sutherland et al. (2017). We also neglect the effects of lateral strain rate variations

10.1029/2020GC008972

Table 1
Effective Closure Temperatures (T_C) as a Function of Cooling Rates for AFT, ZFT, ZHe, and AHe thermochronometers, Adopted From Reiners and Brandon (2006)

Cooling rates (°C/Myr)	AFT (°C)	ZFT (°C)	ZHe (°C)	AHe (°C)
0.1	80	190	140	40
1.0	100	210	160	50
10.0	120	230	180	60
100.0	140	260	210	80

in our models. We assume the orogen to be in topographic steady state, such that rock uplift rates are equal to the exhumation rates, which is appropriate for uplifting regions with high erosion rates (Adams, 1981; Herman et al., 2007, 2009).

The 1-D temperature-depth profile is governed by the following second-order differential equation:

$$k\frac{d^2T}{dz^2} + Cv\frac{dT}{dz} + H = C\frac{dT}{dt} \tag{2}$$

Here z is the depth, k is the thermal conductivity, C is the volumetric heat capacity, H is the volumetric heat productivity, v is the exhumation rate, T is the temperature, and t is the time. Solutions of the 1-D thermal structure depth profile were obtained numerically and analytically (see supporting information).

We employ the following boundary conditions and parameter values:

1. A thermal conductivity of 3.2 W m^{-1} K^{-1}, a volumetric heat productivity of 3.0×10^{-6} W m^{-3} and a thermal diffusivity of 2.0×10^{-6} m^2 s^{-1}, respectively, measured on rock samples from typical lithologies of the Alpine Fault hanging wall (Janku-Čápová, 2018);
2. A temperature of $T_0 = 13$°C at sea level, which is close to the mean annual temperature and imposed as the upper boundary condition (Sutherland et al., 2009; Upton & Sutherland, 2014);
3. A temperature of $T_{BDT} = 450$°C, at the brittle-ductile transition zone (Sibson, 1984; Scholz, 1988), although this restriction is removed in later models;
4. A décollement depth of $Z_{BASE} = 35$ km, imaged with geophysical techniques during the SIGHT experiment (Davey et al., 2007; Stern et al., 2007); and
5. A temperature of $T_{BASE} = 550$°C for the depth of the décollement, based on thermobarometric estimates from high-grade mylonites exhumed in the hanging wall from the lower part of the crust due to the convergent component of slip (Norris & Toy, 2014; Toy et al., 2008, 2010; Upton et al., 1995; Vry et al., 2004).

Temperature profiles are illustrated for various uplift rates in Figure 4a. The general shapes of the temperature profiles derived here (Figure 4a) are consistent with those obtained in previous studies (Cross et al., 2015; Koons, 1987; Toy et al., 2010). These profiles exhibit a high upper-crustal geothermal gradient and a lower geothermal gradient in the deeper parts of the crust as expected given the imposed boundary conditions and parameter values. The profiles corresponding to rapid uplift rates exhibit an inverted shape in the deeper parts of the model (Figure 4a) due to heat production occurring during advection (cf. Koons, 1987). This thermal feature of the model is consistent with prograde metamorphism during advection (e.g., fluid inclusions and the peak temperature of ductile deformation; Toy et al., 2008; Upton et al., 1995). Figure 4b shows the temporal response to exhumation rate change. The initial condition represents a stable crust without exhumation, based on the heat production value mentioned above. Geotherms after 5 Myr are very similar to the steady-state one.

2.4. Regional Exhumation Rates

We next calculate models of the crustal thermal structure compatible with the 45 seismicity cutoff estimates and 150 thermochronological observations. A significant advantage of incorporating the thermochronological information in our models is that the models will be consistent with long-term vertical kinematics of the orogen. Additionally, because the thermochronometers are independently estimated based on their corresponding closure temperatures, we can solve for the T_{BDT} temperature as well as for the exhumation rates.

We define a grid of 55 points, formed by five lines of 11 points parallel to the Alpine Fault, spaced 20 km apart (Figure S6 of the supporting information). We use a relatively coarse grid for simplicity. The 22 points at the northwestern-most and southeastern-most lines are assigned fixed exhumation rates of 0.1 mm/yr, and the 33 points in the interior have adjustable exhumation rate parameters. The model has 34 adjustable parameters (i.e., the T_{BDT} parameter and the exhumation rate at the 33 interior grid points) and two fixed parameters that are based on independent geological and geophysical studies ($Z_{BASE} = 35$ km,

10.1029/2020GC008972

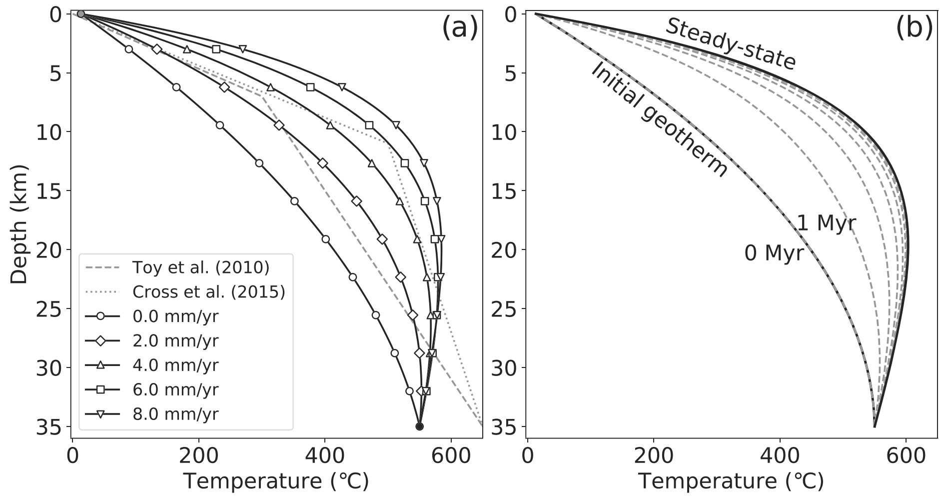

Figure 4. (a) Temperature versus depth profiles for an exhuming block in the central Southern Alps region for varying exhumation rate values (0, 2, 4, 6, and 8 mm/yr). Grey and black dots represent the boundary conditions imposed at the surface and the décollement, respectively. Previous temperature profiles from Cross et al. (2015) and Toy et al. (2010) are also shown as grey dotted and dashed lines, respectively. (b) Temperature versus depth profiles as a function of time in 1 Myr intervals for exhumation at a constant rate of 8 mm/yr. The solid black lines represent the two end-member assumptions (unperturbed initial geotherm versus steady-state geotherm).

T_{BASE} = 550°C; Davey et al., 2007; Stern et al., 2007; Toy et al., 2010; Vry et al., 2004) and the low exhumation rates imposed along the northwest and southeast boundaries.

We interpolate exhumation rate between grid nodes using a linear interpolation method. By doing so, we can compute a 1-D thermal history and current thermal profile using the exhumation rate v^{pred} at any given location within the limits of the grid. At the location of each thermochronological observation, we use the thermal profile (either initial or steady state) to calculate an effective closure depth, Z_c, given the effective closure temperature. We calculate the predicted age, A^{pred}, using the following equation:

$$A^{pred} = \frac{Z_c + Y}{v^{pred}} \tag{3}$$

where Y is the elevation at which the thermochronological sample was collected (required because we assume topography above sea level that does not affect isotherms at greater depths). The thermochronological observations misfit, Q_T, is then calculated via

$$Q_T = \sum_{j=1}^{m} \frac{\left(A_j^{obs} - A_j^{pred}\right)^2}{\sigma_j^2} \tag{4}$$

Here m is the number of thermochronological observations (150) and σ_j is the error measurement of each observation (which includes local spatial variability of observations; see Equation 1). The normalized residuals of the thermochronological observations, R_T, are calculated according to the following equation:

$$R_T = \frac{\left(A_j^{obs} - A_j^{pred}\right)}{\sigma_j} \tag{5}$$

Similarly, at the location of each seismicity observation, we use the interpolated exhumation rate to estimate the temperature profile and obtain the predicted depth of the brittle-ductile transition (BDT), Z^{pred}, according to the value of T_{BDT} that is adjusted during successive iterations of the optimization procedure. As noted above, we do not consider the effects of lateral strain rate variations when calculating Z^{pred}. We calculate the misfit between observed and predicted brittle-ductile depths as

$$Q_S = \sum_{i=1}^{n} \frac{\left(Z_i^{obs} - Z_i^{pred}\right)^2}{\sigma_i^2} \tag{6}$$

where n is the number of seismicity observations (45) and σ_i is the the 1σ error of $Z_i^{obs} = z_0$ (the line fitting the cumulative distribution of the hypocentral depths; section 2.1.1). The normalized residuals of the seismicity observations, R_S, are calculated similarly following equation:

$$R_S = \frac{\left(Z_j^{obs} - Z_i^{pred}\right)}{\sigma_i} \tag{7}$$

To compute the total misfit in each iteration of the optimization process, we must combine two different types of datasets and their corresponding uncertainties. Both seismicity and thermochronological uncertainties are estimated taking into account the lateral variability of their measurements but using different approaches, as described above, due to the difference in the size of datasets (i.e., several thousands for the seismicity to a couple of hundreds for the thermochronological). In order to cope with the discrepancy between the nature of the uncertainties of the two different datasets, we introduce a regularization parameter α that controls the weight attached to the two types of misfits when minimizing the total misfit Q, such that

$$Q = \alpha Q_T + Q_S \tag{8}$$

We consider three different models corresponding to different values of α (two for steady-state conditions and one assuming an initial state for the thermochronological data). The first model is constrained by seismicity cutoff depths only (i.e., $\alpha = 0$). The second model has $\alpha = 1.0$, meaning that both datasets have equal weight. Finally, the third model also has $\alpha = 1.0$ and assumes an initial geotherm (stable crust) established before exhumation of the Southern Alps orogen started. Therefore, in this model when calculating the temperature-depth profile used to find the effective closure depth for the thermochronological data, the exhumation rate is set to zero. Additional models with α values of between 0 and 1.0 were also considered and are presented in the supporting information (Figures S7 and S8) but lead us to similar conclusions. In particular, we considered $\alpha = n/m$, which removes the weight from the different number of observations, and $\alpha = Q_S/Q_T$, which normalizes the different types of uncertainties and the different number of observations in the two datasets.

3. Results

3.1. Exhumation Rates Based on Seismicity

As an initial model, we only use seismicity observations to obtain estimates of exhumation rates, meaning that $\alpha = 0$ in Equation 8. We use the lower seismicity cutoff depth values (z_0) and assume that they correspond to the brittle-ductile transition at $T_{BDT} = 450°$ C and that exhumation is at steady state. The z_0 values are calculated following the analysis described in section 2.1.1.

Setting $T = T_{BDT}$ and $Z = z_0$ we solve for the exhumation rate, v. For the assumed T_{BDT} temperature of 450°C, we obtain an exhumation rate estimate for each bin containing more than 30 earthquakes that lies in the hanging wall of the Alpine Fault. We exclude bins on the periphery of the seismic network (bins 5, 6, 26, 29, 62, and 76; Figure S1).

The exhumation rates obtained from the seismicity cutoff depths alone vary from 1 to 11 mm/yr (Figure 5). We observe the highest exhumation rates (>6 mm/yr) in the vicinity of Aoraki/Mount Cook. These exhumation rates are in close agreement with the youngest hornblende cooling ages related to exhumation rates of as much as ~6–9 mm/yr by Little et al. (2005). A noteworthy aspect of Figure 5 is the large difference in exhumation rates (~8 mm/yr) over a relatively short along-strike distance (<100 km) of the Alpine Fault.

3.2. Exhumation Rates Computed from Seismicity and Thermochronological Data

Figure 6 shows the distribution of the exhumation rate estimates obtained for the models computed using both seismicity and thermochronological observations. These models are based upon two end-member assumptions (i.e., a steady-state exhumation geotherm Figure 6a and an initial stable geotherm with a

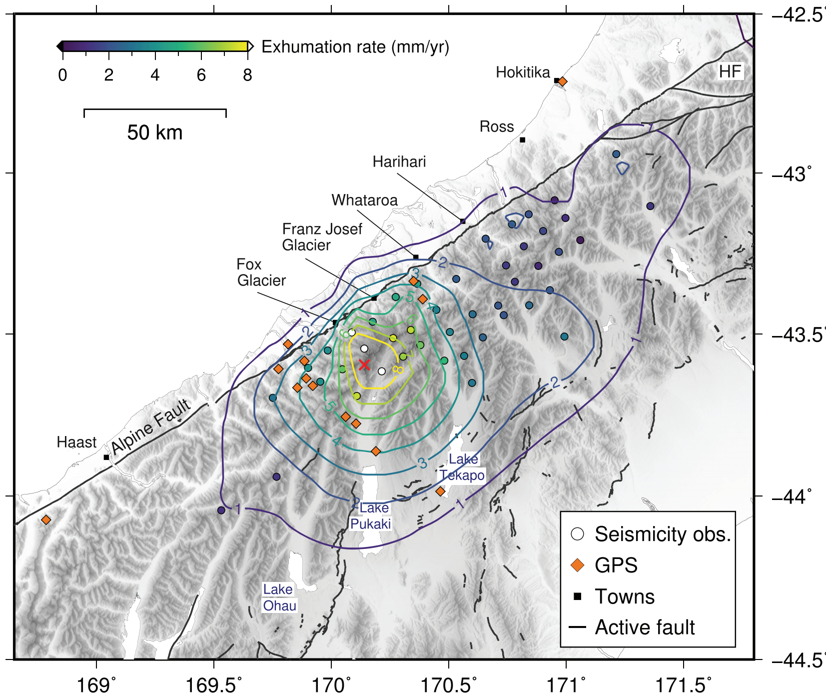

Figure 5. Contoured distribution of the exhumation rates in the central Southern Alps based on seismicity cutoff depths and assuming that the base of the seismicity corresponds to a temperature T_{BDT} = 450°C. Circles represent the uplift rate calculations obtained from the bins defined in Figure S1 containing at least 30 observations, and their colors denote the uplift rate values. Orange diamonds mark the positions of GPS sites. Aoraki/Mount Cook is represented by a red cross. Black lines show active faults from the New Zealand Active Faults Database (http://data.gns.cri.nz/af/). HF is the Hope Fault.

non-exhuming crust Figure 6b) and yield similar exhumation rate patterns. Thus, modeling the temperature-time histories of individual thermochronological observations would not dramatically change the inferred spatial exhumation patterns.

Exhumation rates vary from 1 to 8 mm/yr along the length of the central Alpine Fault, with the highest values (6–8 mm/yr) observed close to Aoraki/Mount Cook. The lowest exhumation rates (<2 mm/yr) are consistently observed in the northeastern part of the study area (near Harihari and Hokitika; Figure 6). In the southwestern part of the model domain (near Haast; Figure 6), exhumation rates are generally <1 mm/yr for the steady-state models computed with different values for α and significantly larger (2–3 mm/yr) in the model incorporating an initial geotherm (exhumation rate = 0.0 mm/yr; Figure 4). The distributions of normalized residuals for both datasets (R_T and R_S; Figure 7) exhibit only local variability in the central part of the examined region, because the models are constrained by many observations in that region. Long-wavelength signals are mostly observed in the periphery of the model grid. Residual values are relatively large which suggests that the grid and smoothing of the parameterization are not able to represent the real exhumation pattern that is more complex. However, since different assumptions all produce similar results, the broader conclusions are unlikely to be affected by this remaining misfit.

3.3. Crustal Thermal Structure, Hypocentral Temperatures, and Geotherms

To calculate the temperature of earthquake hypocenters, the steady-state exhumation assumption is used to estimate the present-day geotherm in all models (Figure 8). This assumption will overestimate the earthquake temperatures (Figure 4b). Nevertheless, geotherms after 3–5 Myr show little to no difference from the steady-state one (10 Ma); therefore, the steady-state assumption is expected to work well (Figure 4b). This occurs because advection and heat production dominate the deep part of the temperature depth profile, and the near-surface boundary layer is relatively thin. Furthermore, the steady-state assumption is also supported by data from Waiho-1 borehole, on the coast approximately 25 km north of Aoraki/Mount Cook, which indicate an onset of exhumation in the middle Miocene and little change in sedimentation since 5 Ma (Sutherland, 1996), whereas in the northern South Island, rapid Alpine exhumation and inversion is clear since 3.6 Ma (Mortimer et al., 2001). Exhumation models also have previously shown rapid exhumation in the central Southern Alps since at least 5 Ma (Jiao et al., 2017; Little et al., 2005; Ring et al., 2019).

We performed a sensitivity analysis on the models considered here (results summarized in Table S1 of the supporting information). We calculated models with varying values for different parameters (e.g., Z_{BASE}; décollement depth, T_{BASE}; temperature at the décollement depth, initial guess for the T_{BDT}). A slightly shallower Z_{BASE} of 30 km gave slightly higher temperatures (10–20°C) than obtained for a Z_{BASE} of 35 km. T_{BDT} estimates generally increase with increasing décollement temperature T_{BASE}. In light of this, our assumption of a T_{BASE} of 550°C provides us with realistic and conservative estimates while still being consistent with with previous analyses by Vry et al. (2004, 2008) and Ring et al. (2019) that suggest slightly higher temperatures at the base of the décollement (i.e., 550–650°).

The estimated temperatures at the brittle-ductile transition (T_{BDT}) are 430±110° C and 410±70° C for the steady-state and initial geotherm models, respectively. These values represent the average and standard deviation of the T_{BDT} estimates obtained for $T_{BASE} = 550$°C and seven different initial values for T_{BDT}. Figure 8 shows the earthquake hypocenter temperatures for one of the steady-state and initial geotherm models considered here (all T_{BDT} estimates are shown in Table S1 of the supporting information).

To examine whether the two different sets of observations used here do not adversely bias the final results, we have also considered two models incorporating solely thermochronological and seismicity observations. The two models gave very similar results (Figure S9 of the supporting information).

Figure 9 shows a cross section of the seismicity hypocenters from the catalog of Michailos et al. (2019) and the 100°C, 200°C, 300°C, 400°C, and 500°C isotherms along cross section A–A′ marked in Figure 6. The distribution of the isotherms depends upon the temperature at the brittle-ductile transition defined by the models. We use the value of T_{BDT} obtained from the steady-state model. We observe close spacing of the isotherms (i.e., high temperature gradients) beneath Aoraki/Mount Cook that are consistent with the shallow seismicity there.

Having established the thermal structure, we can estimate geothermal gradients at the locations of each earthquake. These range from 16 to 74°C/km, with the highest values coinciding with the areas of highest relief and shallow seismicity cutoff depths. Temperature measurements made in the DFDP-1B borehole at Gaunt Creek (62.6±2.1° C/km; Sutherland et al., 2012) lie within our modeled estimates here. However, our geothermal gradient estimates do not agree with the extreme geothermal gradient of 125±55° C/km observed in the DFDP-2B borehole at Whataroa Valley (Sutherland et al., 2017). This difference in the geothermal gradient near Whataroa is due to the local topographically driven fluid movement that concentrates heat in the valleys (Sutherland et al., 2017; Townend et al., 2017), a feature that we have not included in our modeling.

4. Discussion

4.1. Comparison With Geologically and Geodetically Determined Uplift Rates

Our exhumation rate findings are consistent with those of Wellman (1979), Tippett and Kamp (1993), and Little et al. (2005), who each inferred rapid uplift and exhumation rates in the central part of the Southern Alps using Quaternary slip rate data and fission-track ages. Little et al. (2005) reported maximum uplift rates of ∼6–9 mm/yr in a small region near Franz-Josef and Fox glaciers, which are in close agreement with our modeled results here. Moreover, our final exhumation estimates (Figure 6) are very similar to the geodetically estimated uplift rates of ∼5 mm/yr obtained by Beavan et al. (2010) along a GPS transect spanning the Southern Alps (Figure 10). The exhumation rate estimates calculated here follow the same pattern as the geodetic observations and have slightly larger values (∼1 mm/yr), but are within the geodetic estimates' confidence limits). These independently estimated geodetic estimates were not incorporated into the modeling process but instead used for post hoc comparison purposes and for validating our estimated exhumation rates.

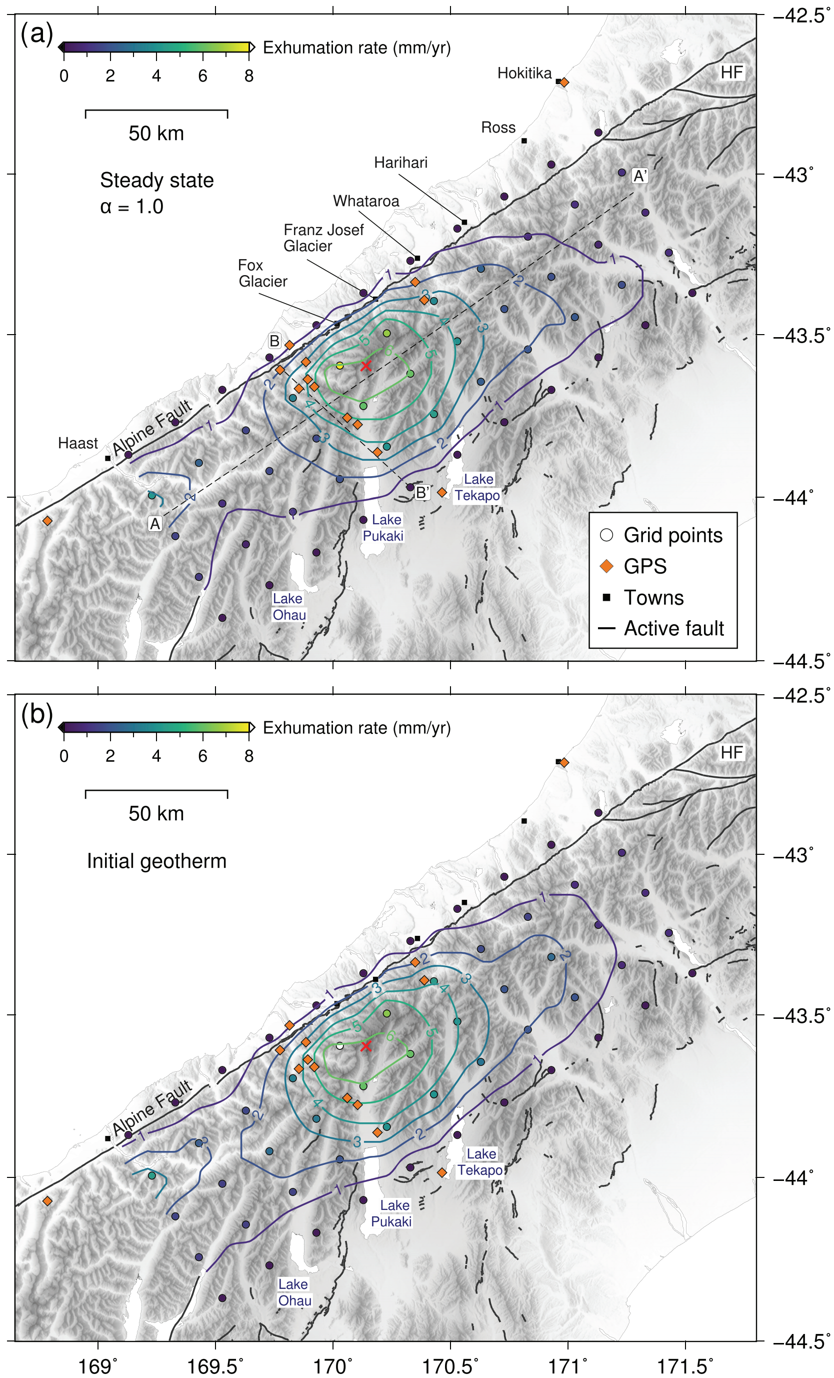

Figure 6. Contoured distribution of the exhumation rates in the central Southern Alps based on seismicity and thermochronological data. (a) Steady-state model ($\alpha = 1.0$) that weights the seismicity and thermochronological observations equally in the optimization process. (b) Initial geotherm (stable crust) model established before the initiation of the exhumation process. Circles represent the modeling grid points, and their colors denote the exhumation rate values. Orange diamonds mark the locations of GPS sites. Aoraki/Mount Cook is represented by a red cross. Black lines show active faults from the New Zealand Active Faults Database (http://data.gns.cri.nz/af/). HF is the Hope Fault.

4.2. Model Misfits

Large model misfit Q values (Equation 8) correspond to relatively large individual normalized residuals >2 (Figure 7). These large residuals arise due to two main reasons. First, the models presented here are simplified and have low spatial resolution and therefore cannot depict the real spatial variation in exhumation

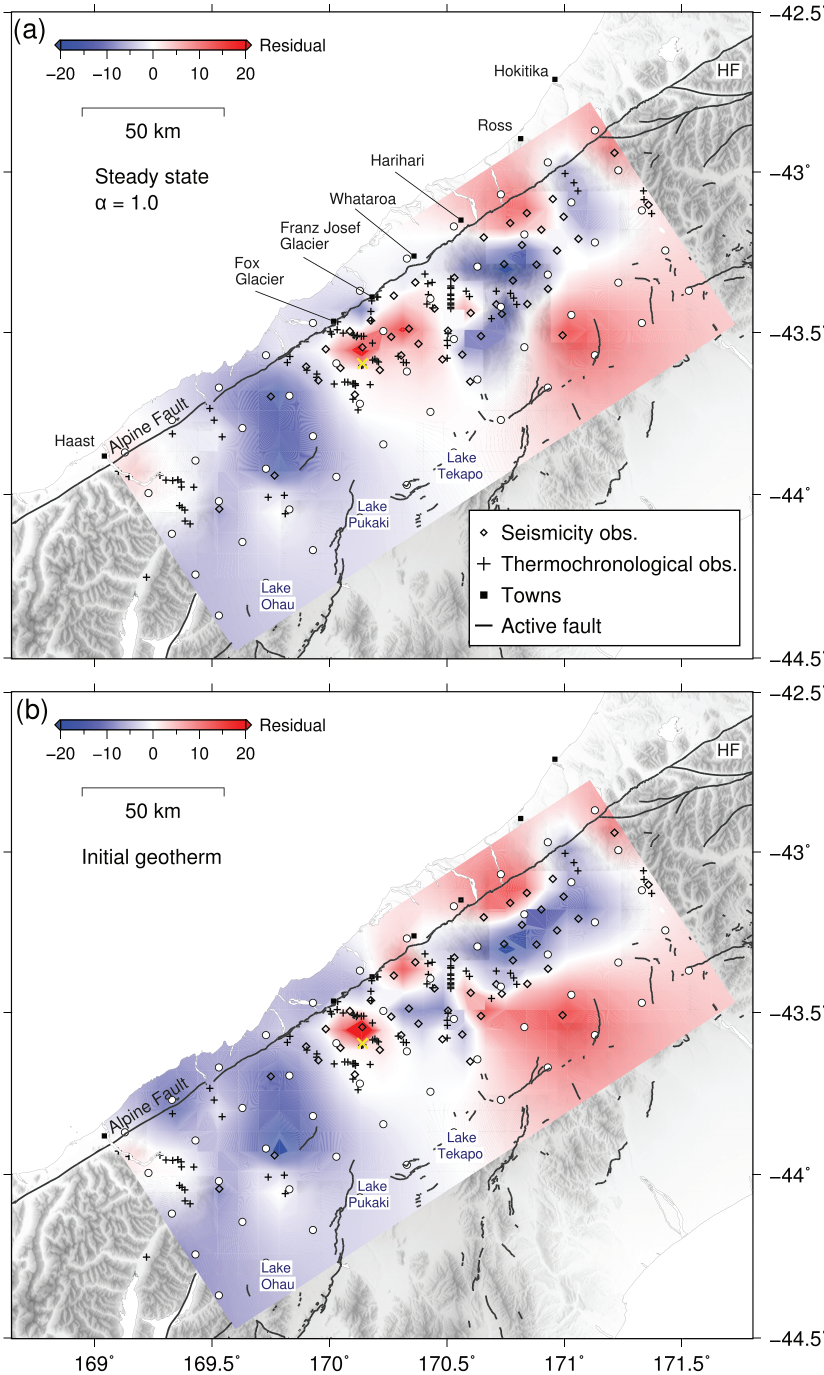

Figure 7. Spatial distribution of the standard residuals of the seismicity and thermochronological observations. (a) Steady-state model ($\alpha = 1.0$) that weights the seismicity and thermochronological observations equally in the optimization process. (b) Initial geotherm (stable crust) model established before the initiation of the exhumation process. Circles represent the modeling grid points. Seismicity and thermochronological data locations are shown with diamonds and crosses, respectively. Aoraki/Mount Cook is represented by a yellow cross. Black lines show active faults from the New Zealand Active Faults Database (http://data.gns.cri.nz/af/). HF is the Hope Fault.

rates caused by processes such as small-scale faulting. Second, the time interval covered by the earthquake data is short. Moreover, assuming an exhumational steady state for the whole of the examined region in the central Southern Alps is simplistic. Steady state has been suggested to apply only locally in the region of rapid exhumation (Allis & Shi, 1995; Koons, 1987). However, the simple crustal thermal structure

10.1029/2020GC008972

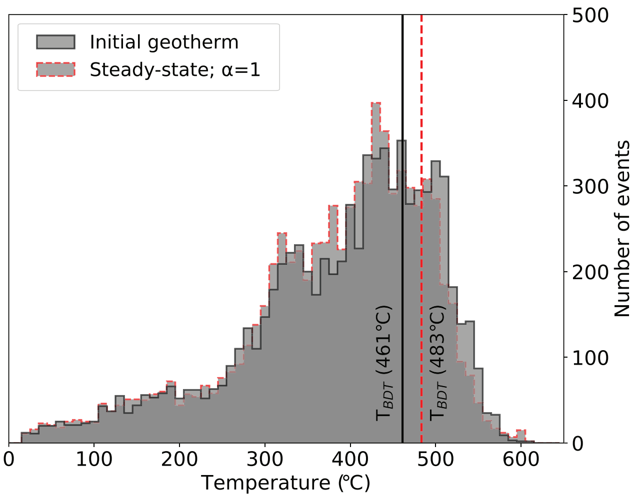

Figure 8. Temperature distribution of individual earthquakes. Histograms of the earthquake temperatures for one of the steady-state ($\alpha = 1.0$) and initial geotherm models considered here are shown with the dashed red line and solid black line, respectively. The temperatures at the brittle-ductile transition (BDT) are also shown for each model.

constructed here can provide a reasonable estimation of the broader picture of the distribution of exhumation rates, which matches the goals of the present work.

4.3. Implications of Relatively Hot Crust

The earthquake hypocenter temperatures and the T_{BDT} estimate obtained from the steady-state and initial geotherm models using both seismicity and thermochronological observations are slightly hotter than expected for crust composed mainly of quartz-rich rocks (i.e., 300–350°C; Sibson, 1984). These relatively hot temperatures are likely overestimated as we have used the steady-state exhumation assumption to compute the current thermal structure. The brittle-ductile transition temperatures are similar to those inferred for a crust consisting of feldspar-rich rocks (i.e., ~450°C; Bonner et al., 2003; Sibson, 1984). Feldspar-rich rocks however are not abundant in the Southern Alps (exhumed Alpine Fault rocks); rather, the typical lithology is quartzo-felspathic (Cox & Barrell, 2007) with quartz present in such proportions that it is probably the rheologically dominant phase.

We estimate that the base of the seismogenic zone in the Southern Alps is hotter by about ~100° C than predicted from a simple quartz-dominated brittle-ductile rheological model, and we offer two possible explanations. First, it may be that fluid pressures at the base of the seismogenic zone are locally close to lithostatic. Based on evidence for abundant upper-crustal fluid circulation (e.g., Menzies et al., 2014, 2016; Sutherland et al., 2017; Townend et al., 2017), it seems likely that most of the crust only deviates slightly from hydrostatic conditions (sufficient to drive flow), but it is possible that pockets of higher fluid pressure are present near the base of the seismogenic zone. The fluid source could be prograde metamorphism during exhumation (Koons et al., 1998; Upton et al., 2003; Vry et al., 2010), and this hypothesis is supported by seismological observations (Boese et al., 2014; Davey et al., 2007; Stern et al., 2001, 2007) and magnetotelluric data

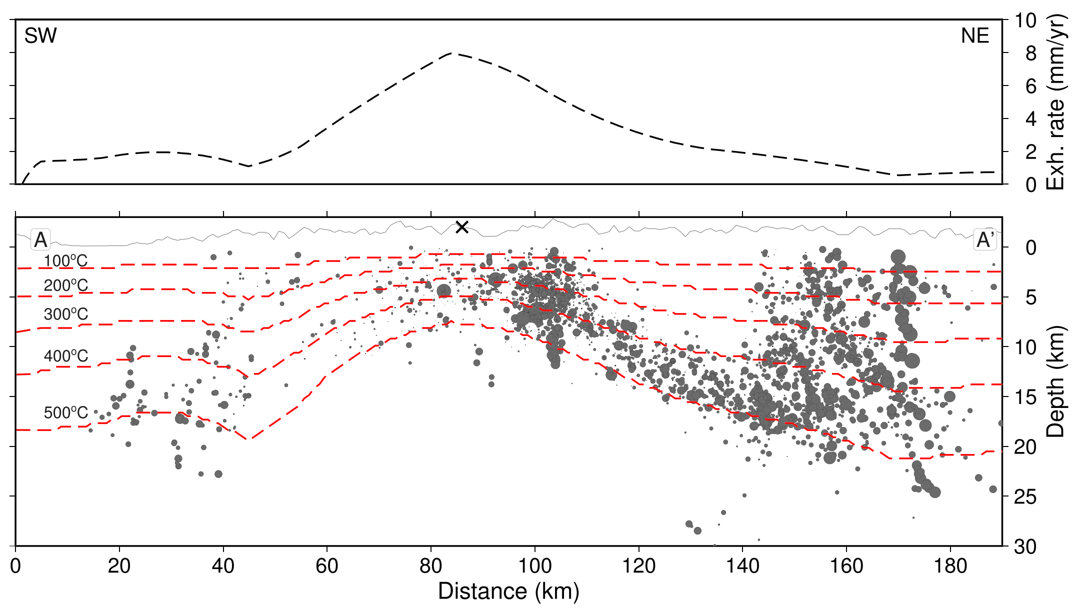

Figure 9. The bottom panel shows a vertical cross-section of earthquake hypocenters and temperature estimates (100°C, 200°C, 300°C, 400°C, and 500°C isotherms) along line A–A′ shown in Figure 6. Earthquakes within 10 km on either side of the cross section are illustrated as circles, scaled by magnitude. The cross indicates the location of Aoraki/Mount Cook. The light gray line depicts topography. The top panel shows the along-strike variation of the exhumation rate estimates (steady-state models; Figure 6) along line A–A′.

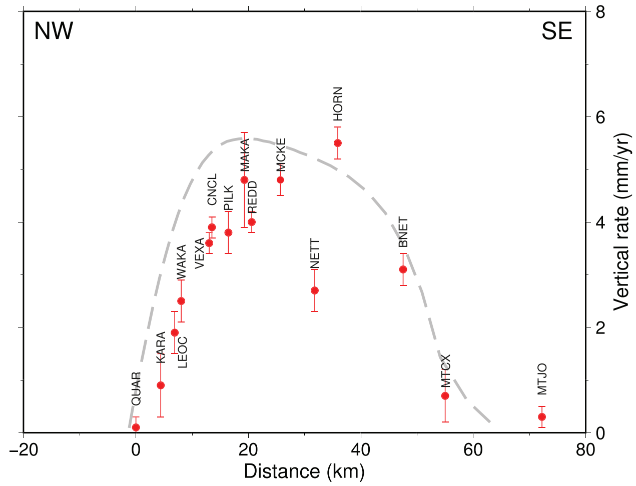

Figure 10. Cross section of interpolated exhumation rate estimates (dashed gray line) from the steady-state model along the GPS transect across the Southern Alps (Beavan et al., 2004). Vertical uplift rate estimates from GPS (red dots with 95% confidence limits) are taken from Table 1 of Beavan et al. (2010). The locations of the permanent GPS sites are shown in Figure 6.

(Wannamaker et al., 2002, 2004, 2009). The second possible explanation is that seismicity at depth is driven by anomalously high strain rates (Bourguignon et al., 2015; Lamb & Smith, 2013; Norris & Cooper, 2007). The base of the seismogenic zone is in close proximity to a plate boundary detachment moving at nearly 40 mm/yr. The width of the detachment zone is a topic of ongoing research (e.g., Warren-Smith et al., 2016), but it is clear that elevated stress is required to deform quartz by deformation creep at rates much higher than normal for the crust (e.g., Sibson, 1984). The occurrence of other aseismic deformation mechanisms, such as pressure solution, might further encourage a deeper transition between seismic and aseismic behaviour (Toy et al., 2010).

The seismicity data used here, despite spanning almost 10 years, only capture a snapshot of the active seismic deformation with respect to the typical seismic cycle of the large Alpine Fault earthquakes (i.e., 250–300 years Berryman et al., 2012; Cochran et al., 2017; Howarth et al., 2016, 2018; Sutherland et al., 2007). Seismicity cutoff depths vary adjacent to a large plate boundary fault throughout the seismic cycle (e.g., Jiang & Lapusta, 2016). Conversely, thermochronological observations do not capture short-term processes or coseismic effects associated with large Alpine Fault earthquakes. Our results show that the two data sets can nevertheless be reconciled with simple thermal models and provide a basis for more detailed analysis of the short- and long-term behaviors of the orogen.

5. Conclusions

We combine two contrasting types of data, seismicity and thermochronological measurements, to construct a thermal model of the crust and estimate exhumation rates in the central Southern Alps. The most significant finding to emerge from modeling performed in this study is that the two datasets give consistent results and show there is considerable spatial variation in exhumation rate (1–8 mm/yr) along the length of the Alpine Fault. Our results are in good agreement with existing geologically (Little et al., 2005) and geodetically (Beavan et al., 2010) determined rates. We estimate the temperature at the lower seismicity cutoff depth to be $T_{BDT} =$ 410–430°C. Such temperatures are higher than expected for quartz-dominated lithologies of the composition of exhumed Alpine Fault rocks (for which T_{BDT} is typically 300–350°C) and may reflect the effects of unmodeled fluid pressures and/or high strain rates.

Acknowledgments

We are grateful to Virginia Toy of Johannes Gutenberg University, Mainz, and an anonymous reviewer for critical comments on our original manuscript. We also acknowledge helpful feedback from Tim Little on an early version of this manuscript. This study was funded by the Marsden Fund of the Royal Society Te Apārangi (13-VUW-101), the Earthquake Commission of New Zealand (EQC Programme in Seismology and Fault Mechanics at Victoria University of Wellington). We used GMT for constructing maps (Wessel et al., 2013) and ObsPy for data processing (Beyreuther et al., 2010; Krischer et al., 2015).

References

Adams, C. J. (1981). Uplift rates and thermal structure in the Alpine Fault Zone and Alpine Schists, Southern Alps, New Zealand. *Geological Society Special Publication*, *9*, 211–222. https://doi.org/10.1144/GSL.SP.1981.009.01.19

Albaric, J., Déverchère, J., Petit, C., Perrot, J., & Le Gall, B. (2009). Crustal rheology and depth distribution of earthquakes: Insights from the central and southern East African Rift System. *Tectonophysics*, *468*(1-4), 28–41. https://doi.org/10.1016/j.tecto.2008.05.021

Allis, R. G., Henley, R. W., & Carman, A. F. (1979). *The thermal regime beneath the Southern Alps*. Wellington: Royal Society of New Zealand.

Allis, R. G., & Shi, Y. (1995). New insights to temperature and pressure beneath the central Southern Alps, New Zealand. *New Zealand Journal of Geology and Geophysics*, *38*(4), 585–592. https://doi.org/10.1080/00288306.1995.9514687

Batt, G. E., & Braun, J. (1999). The tectonic evolution of the Southern Alps, New Zealand: Insights from fully thermally coupled dynamical modelling. *Geophysical Journal International*, *136*(2), 403–420. https://doi.org/10.1046/j.1365-246X.1999.00730.x

Batt, G. E., Braun, J., Kohn, B., & McDougall, I. (2000). Thermochronological analysis of the dynamics of the Southern Alps, New Zealand. *Bulletin of the Geological Society of America*, *112*(2), 250–266.

Beavan, J., Denys, P., Denham, M., Hager, B., Herring, T., & Molnar, P. (2010). Distribution of present-day vertical deformation across the Southern Alps, New Zealand, from 10 years of GPS data. *Geophysical Research Letters*, *37*, L16305. https://doi.org/10.1029/2010GL044165

Beavan, J., Ellis, S., Wallace, L., & Denys, P. (2007). Kinematic constraints from GPS on oblique convergence of the Pacific and Australian plates, central South Island, New Zealand. *Washington DC American Geophysical Union Geophysical Monograph Series*, *175*, 75–94.

Beavan, J., Matheson, D., & Denys, P. (2004). A vertical deformation profile across the Southern Alps, New Zealand, from 3.5 years of continuous GPS data. *Proceedings of the Cahiers du Centre Européen de Géodynamique et de Séismologie workshop: The State of GPS Vertical Positioning Precision: Separation of Earth Processes by Space Geodesy, Luxembourg*, *23*, 111–123.

Beavan, J., Moore, M., Pearson, C., Henderson, M., Parsons, B., Bourne, S., et al. (1999). Crustal deformation during 1994–1998 due to oblique continental collision in the central Southern Alps, New Zealand, and implications for seismic potential of the Alpine Fault. *Journal of Geophysical Research*, *104*(B11), 25,233–25,255. https://doi.org/10.1029/1999JB900198

Beeler, N. M., Hirth, G., Tullis, T. E., & Webb, C. H. (2018). On the depth extent of coseismic rupture. *Bulletin of the Seismological Society of America*, *108*(2), 761–780. https://doi.org/10.1785/0120160295

Berryman, K. R., Cochran, U. A., Clark, K. J., Biasi, G. P., Langridge, R. M., & Villamor, P. (2012). Major earthquakes occur regularly on an isolated plate boundary fault. *Science*, *336*(6089), 1690–1693. https://doi.org/10.1126/science.1218959

Beyreuther, M., Barsch, R., Krischer, L., Megies, T., Behr, Y., & Wassermann, J. (2010). ObsPy: A Python toolbox for seismology. *Seismological Research Letters*, *81*(3), 530–533. https://doi.org/10.1785/gssrl.81.3.530

Boese, C. M., Jacobs, K. M., Smith, E. G. C., Stern, T. A., & Townend, J. (2014). Background and delayed-triggered swarms in the central Southern Alps, South Island, New Zealand. *Geochemistry, Geophysics, Geosystems*, *15*, 945–964. https://doi.org/10.1002/2013GC005171

Boese, C. M., Townend, J., Smith, E., & Stern, T. (2012). Microseismicity and stress in the vicinity of the Alpine Fault, central Southern Alps, New Zealand. *Journal of Geophysical Research*, *117*, B02302. https://doi.org/10.1029/2011JB008460

Bonner, J. L., Blackwell, D. D., & Herrin, E. T. (2003). Thermal constraints on earthquake depths in California. *Bulletin of the Seismological Society of America*, *93*(6), 2333–2354. https://doi.org/10.1785/0120030041

Bourguignon, S., Bannister, S., Henderson, C. M., Townend, J., & Zhang, H. (2015). Structural heterogeneity of the midcrust adjacent to the central Alpine Fault, New Zealand: Inferences from seismic tomography and seismicity between Harihari and Ross. *Geochemistry, Geophysics, Geosystems*, *16*, 1017–1043. https://doi.org/10.1002/2014GC005702

Cande, S. C., & Stock, J. M. (2004). Pacific-Antarctic-Australia motion and the formation of the Macquarie Plate. *Geophysical Journal International*, *157*(1), 399–414. https://doi.org/10.1111/j.1365-246X.2004.02224.x

Chen, W.-P., & Molnar, P. (1983). Focal depths of intracontinental and intraplate earthquakes and their implications for the thermal and mechanical properties of the lithosphere. *Journal of Geophysical Research*, *88*, 4183–4214.

Cochran, U. A., Clark, K. J., Howarth, J. D., Biasi, G. P., Langridge, R. M., Villamor, P., et al. (2017). A plate boundary earthquake record from a wetland adjacent to the Alpine Fault in New Zealand refines hazard estimates. *Earth and Planetary Science Letters*, *464*, 175–188. https://doi.org/10.1016/j.epsl.2017.02.026

Cox, S. C., & Barrell, D. J. A. (2007). Geology of the Aoraki area. Lower Hutt: GNS Science. Institute of Geological & Nuclear Sciences 1:250,000 geological map 15. 71 p. + 1 folded map.

Cox, S. C., Menzies, C. D., Sutherland, R., Denys, P. H., Chamberlain, C., & Teagle, D. A. H. H. (2015). Changes in hot spring temperature and hydrogeology of the Alpine Fault hanging wall, New Zealand, induced by distal South Island earthquakes. *Geofluids*, *15*, 216–239. https://doi.org/10.1111/gfl.1209

Cross, A. J., Kidder, S., & Prior, D. J. (2015). Using microstructures and TitaniQ thermobarometry of quartz sheared around garnet porphyroclasts to evaluate microstructural evolution and constrain an Alpine Fault Zone geotherm. *Journal of Structural Geology*, *75*, 17–31. https://doi.org/10.1016/j.jsg.2015.02.012

Davey, F. J., Eberhart-Phillips, D., Kohler, M. D., Bannister, S., Caldwell, G., Henrys, S., et al. (2007). Geophysical structure of the Southern Alps orogen, South Island, New Zealand. In D. Okaya, T. Stern, & F. Davey (Eds.), *A continental plate boundary: Tectonics at South Island, New Zealand* (Vol. 175, pp. 47–73). Washington, DC: American Geophysical Union. https://doi.org/10.1029/175GM04

Davey, F. J., Henyey, T., Kleffman, S., Melhuish, A., Okaya, D., Stern, T. A., & Group, SIGTSIGHT (1995). Crustal reflections from the Alpine Fault Zone, South Island, New Zealand. *New Zealand Journal of Geology and Geophysics*, *38*(4), 601–604. https://doi.org/10.1080/00288306.1995.9514689

DeMets, C., Gordon, R. G., & Argus, D. F. (2010). Geologically current plate motions. *Geophysical Journal International*, *181*(1), 1–80. https://doi.org/10.1111/j.1365-246X.2009.04491.x

Dodson, H. M. (1973). Closure temperature in cooling geochronological and petrological systems. *Contributions to Mineralogy and Petrology*, *40*, 259–274. https://doi.org/10.1007/BF00373790

Doser, D. I., & Kanamori, H. (1986). Depth of seismicity in the Imperial Valley region (1977–1983) and its relationship to heat flow. *Journal of Geophysical Research*, *91*(5), 675–688. https://doi.org/10.1029/JB091iB01p00675

Gleadow, A. J. W., & Duddy, I. R. (1981). A natural long-term track annealing experiment for apatite. *Nuclear Tracks*, *5*(1-2), 169–174. https://doi.org/10.1016/0191-278X(81)90039-1

Hauksson, E., & Meier, M.-A. (2018). Applying depth distribution of seismicity to determine thermo-mechanical properties of the seismogenic crust in southern California: Comparing lithotectonic blocks. *Pure and Applied Geophysics*, *176*, 1061–1081. https://doi.org/10.1007/s00024-018-1981-z

Herman, F., Braun, J., & Dunlap, W. J. (2007). Tectonomorphic scenarios in the Southern Alps of New Zealand. *Journal of Geophysical Research*, *112*, B04201. https://doi.org/10.1029/2004JB003472

Herman, F., Cox, S. C., & Kamp, P. J. J. (2009). Low-temperature thermochronology and thermokinematic modeling of deformation, exhumation, and development of topography in the central Southern Alps, New Zealand. *Tectonics*, *28*, TC5011. https://doi.org/10.1029/2008TC002367

Howarth, J. D., Cochran, U. A., Langridge, R. M., Clark, K., Fitzsimons, S. J., Berryman, K., et al. (2018). Past large earthquakes on the Alpine Fault: Paleoseismological progress and future directions. *New Zealand Journal of Geology and Geophysics*, *0*(0), 1–20. https://doi.org/10.1080/00288306.2018.1464658

Howarth, J. D., Fitzsimons, S. J., Norris, R. J., Langridge, R., & Vandergoes, M. J. (2016). A 2000 yr rupture history for the Alpine fault derived from Lake Ellery, South Island, New Zealand. *Bulletin of the Geological Society of America*, *128*(3-4), 627–643. https://doi.org/10.1130/B31300.1

Jackson, J. (2002). Strength of the continental lithosphere: Time to abandon the jelly sandwich? *GSA Today*, *12*, 4–10.

Janku-Čápová, L. (2018). Thermal and hydraulic characterization of the hanging-wall of the central Alpine Fault (Ph.D. Thesis), Victoria University of Wellington.

Jiang, J., & Lapusta, N. (2016). Deeper penetration of large earthquakes on seismically quiescent faults. *Science*, *352*(6291), 1293–1297. https://doi.org/10.1126/science.aaf1496

Jiao, R., Herman, F., & Seward, D. (2017). Late Cenozoic exhumation model of New Zealand: Impacts from tectonics and climate. *Earth-Science Reviews*, *166*, 286–298. https://doi.org/10.1016/j.earscirev.2017.01.003

Kamp, P. J. J., Green, P. F., & White, S. H. (1989). Fission track analysis reveals character of collisional tectonics in New Zealand. *Tectonics*, *8*(2), 169–195.

Kidder, S., Toy, V., Prior, D., Little, T., Khan, A., & Macrae, C. (2018). Constraints on Alpine Fault (New Zealand) mylonitization temperatures and geothermal gradient from Ti-in-quartz thermobarometry. *Solid Earth*, *9*(5), 1123–1139. https://doi.org/10.5194/se-9-1123-2018

Koons, P. O. (1987). Some thermal and mechanical consequences of rapid uplift: An example from the Southern Alps, New Zealand. *Earth and Planetary Science Letters*, *86*(2-4), 307–319. https://doi.org/10.1016/0012-821X(87)90228-7

Koons, P. O., Craw, D., Cox, S. C., Upton, P., Templeton, A. S., & Chamberlain, C. P. (1998). Fluid flow during active oblique convergence: A Southern Alps model from mechanical and geochemical observations. *Geology*, *26*(2), 159–162.

Koons, P. O., Norris, R. J., Craw, D., & Cooper, A. F. (2003). Influence of exhumation on the structural evolution of transpressional plate boundaries: An example from the Southern Alps, New Zealand. *Geology*, *31*(1), 3–6.

Krischer, L., Megies, T., Barsch, R., Beyreuther, M., Lecocq, T., Caudron, C., & Wassermann, J. (2015). ObsPy: A bridge for seismology into the scientific Python ecosystem. *Computational Science and Discovery*, *8*(1), 17. https://doi.org/10.1088/1749-4699/8/1/014003

Lamb, S., & Smith, E. (2013). The nature of the plate interface and driving force of interseismic deformation in the New Zealand plate-boundary zone, revealed by the continuous GPS velocity field. *Journal of Geophysical Research: Solid Earth*, *118*, 3160–3189. https://doi.org/10.1002/jgrb.50221

Leitner, B., & Eberhart-Phillips, D. (2001). A focused look at the Alpine fault, New Zealand: Seismicity, focal mechanisms, and stress observations. *Journal of Geophysical Research*, *106*(2000), 2193–2220.

Little, T. A., Cox, S., Vry, J. K., & Batt, G. (2005). Variations in exhumation level and uplift rate along the oblique-slip Alpine fault, central Southern Alps, New Zealand. *Bulletin of the Geological Society of America*, *117*(5-6), 707–723. https://doi.org/10.1130/B25500.1

Magistrale, H., & Zhou, H. (1996). Lithologic control of the depth of earthquakes in Southern California. *Science*, *273*(5275), 639–642. https://doi.org/10.1126/science.273.5275.639

Menzies, C. D., Teagle, D. A. H., Craw, D., Cox, S. C., Boyce, A. J., Barrie, C. D., & Roberts, S. (2014). Incursion of meteoric waters into the ductile regime in an active orogen. *Earth and Planetary Science Letters*, *399*, 1–13. https://doi.org/10.1016/j.epsl.2014.04.046

Menzies, C. D., Teagle, D. A. H., Niedermann, S., Cox, S. C., Craw, D., Zimmer, M., et al. (2016). The fluid budget of a continental plate boundary fault: Quantification from the Alpine Fault, New Zealand. *Earth and Planetary Science Letters*, *445*, 125–135. https://doi.org/10.1016/j.epsl.2016.03.046

Michailos, K., Smith, E. G. C., Chamberlain, C. J., Savage, M. K., & Townend, J. (2019). Variations in seismogenic thickness along the central Alpine Fault, New Zealand, revealed by a decade's relocated microseismicity. *Geochemistry Geophysics Geosystems*, *20*, 470–486. https://doi.org/10.1029/2018GC007743

Mortimer, N., Sutherland, R., & Nathan, S. (2001). Torlesse greywacke and Haast Schist source for Pliocene conglomerates near Reefton, New Zealand. *New Zealand Journal of Geology and Geophysics*, *44*(1), 105–111. https://doi.org/10.1080/00288306.2001.9514927

Norris, R. J., & Cooper, A. F. (2001). Late Quaternary slip rates and slip partitioning on the Alpine Fault, New Zealand. *Journal of Structural Geology*, *23*(2-3), 507–520. https://doi.org/10.1016/S0191-8141(00)00122-X

Norris, R. J., & Cooper, A. F. (2007). The Alpine Fault, New Zealand: Surface geology and field relationships. In D. Okaya T. Stern & F. Davey (Eds.), *A continental plate boundary: Tectonics at South Island, New Zealand*, *Geophysical Monograph Series* (Vol. 175, pp. 157–175). Washington, DC: American Geophysical Union. https://doi.org/10.1029/175GM09

Norris, R. J., & Toy, V. G. (2014). Continental transforms: A view from the Alpine Fault. *Journal of Structural Geology*, *64*, 3–31. https://doi.org/10.1016/j.jsg.2014.03.003

Peyton, S. L., & Carrapa, B. (2013). An introduction to low-temperature thermochronologic techniques, methodology, and applications. In C. Knight & J. Cuzella (Eds.), *Application of structural methods to Rocky Mountain hydrocarbon exploration and development: AAPG Studies in Geology* (Vol. 65, pp. 15–36). https://doi.org/10.1306/13381688St653578

Reiners, P. W., & Brandon, M. T. (2006). Using thermochronology to understand orogenic erosion. *Annual Review of Earth and Planetary Sciences*, *34*(1), 419–466. https://doi.org/10.1146/annurev.earth.34.031405.125202

Reiners, P. W., Spell, T. L., Nicolescu, S., & Zanetti, K. A. (2004). Zircon (U-Th)/He thermochronometry: He diffusion and comparisons with $^{40}Ar/^{39}Ar$ dating. *Geochimica et Cosmochimica Acta*, *68*(8), 1857–1887. https://doi.org/10.1016/j.gca.2003.10.021

Ring, U., & Bernet, M. (2010). Fission-track analysis unravels the denudation history of the Bonar Range in the footwall of the Alpine Fault, South Island, New Zealand. *Geological Magazine*, *147*(6), 801–813. https://doi.org/10.1017/S0016756810000208

Ring, U., Glodny, J., Angiboust, S., Little, T., & Lang, K. A. (2019). Middle to Late Miocene age for the end of amphibolite-facies mylonitization of the Alpine Schist, New Zealand: Implications for onset of transpression across the Alpine Fault. *Tectonics*, *38*, 4335–4359. https://doi.org/10.1029/2019TC005577

Scholz, C. H. (1988). The brittle-plastic transition and the depth of seismic faulting. *Geologische Rundschau*, *77/1*, 319–328.

Scholz, C. H. (1998). Earthquakes and friction laws. *Nature*, *391*(6662), 37–42. https://doi.org/10.1038/34097

Scholz, C. H. (2002). *The mechanics of earthquakes and faulting* (2nd ed.). Cambridge: Cambridge University Press. https://doi.org/10.1017/CBO9780511818516

Seward, D. (1989). Cenozoic basin histories determined by fission-track dating of basement granites, South Island, New Zealand. *Chemical Geology: Isotope Geoscience Section*, *79*(1), 31–48. https://doi.org/10.1016/0168-9622(89)90005-5

Shaw, B. E., & Wesnousky, S. G. (2008). Slip-length scaling in large earthquakes: The role of deep-penetrating slip below the seismogenic layer. *Bulletin of the Seismological Society of America*, *98*(4), 1633–1641. https://doi.org/10.1785/0120070191

Shi, Y., Allis, R., & Davey, F. (1996). Thermal modeling of the Southern Alps, New Zealand. *Pure and Applied Geophysics PAGEOPH*, *146*(3/4), 469–501. https://doi.org/10.1007/bf00874730

Sibson, R. H. (1982). Fault zone models, heat flow, and the depth distribution of earthquakes in the continental crust of the United States. *Bulletin of the Seismological Society of America*, *72*(1), 151–163.

Sibson, R. H. (1983). Continental fault structure and the shallow earthquake source. *Journal of the Geological Society London*, *140*(5), 741–767. https://doi.org/10.1144/gsjgs.140.5.0741

Sibson, R. H. (1984). Roughness at the base of the seismogenic zone: Contributing factors. *Journal of Geophysical Research*, *89*(B7), 5791–5799. https://doi.org/10.1029/JB089iB07p05791

Stern, T. A., Kleffmann, S., Scherwath, M., Okaya, D., & Bannister, S. (2001). Low seismic wave speeds and enhanced fluid pressures beneath the Southern Alps of New Zealand. *Geology*, *29*, 679–682.

Stern, T. A., Okaya, D., Kleffmann, S., Scherwath, M., Henrys, S., & Davey, F. (2007). Geophysical exploration and dynamics of the Alpine fault zone, *175*, 207–233. https://doi.org/10.1029/175GM11

Sutherland, R. (1995). The Australian-Pacific boundary and Cenozoic plate motions in the SW Pacific. *Tectonics*, *14*(4), 819–831.

Sutherland, R. (1996). Transpressional development of the Australia-Pacific boundary through southern South Island, New Zealand: Constraints from Miocene-Pliocene sediments, Waiho-1 borehole, South Westland. *New Zealand Journal of Geology and Geophysics*, *39*(2), 251–264. https://doi.org/10.1080/00288306.1996.9514709

Sutherland, R. (1999). Cenozoic bending of New Zealand basement terranes and Alpine Fault displacement: A brief review. *New Zealand Journal of Geology and Geophysics*, *42*(2), 295–301. https://doi.org/10.1080/00288306.1999.9514846

Sutherland, R., Eberhart-Phillips, D., Harris, R. A., Stern, T. A., Beavan, R. J., Ellis, S., et al. (2007). Do great earthquakes occur on the Alpine Fault in central South Island, New Zealand? *A Continental Plate Boundary: Tectonics at South Island, New Zealand*, *175*, 235–251. https://doi.org/10.1029/175GM12

Sutherland, R., Gurnis, M., Kamp, P. J. J., & House, M. A. (2009). Regional exhumation history of brittle crust during subduction initiation, Fiordland, southwest New Zealand, and implications for thermochronologic sampling and analysis strategies. *Geosphere*, *5*(5), 409–425. https://doi.org/10.1130/GES00225.SA2

Sutherland, R., Townend, J., Toy, V., Upton, P., Coussens, J., Allen, M., et al. (2017). Extreme hydrothermal conditions at an active plate-bounding fault. *Nature*, *546*(7656), 137–140. http://dx.doi.org/10.1038/nature22355

Sutherland, R., Toy, V. G., Townend, J., Cox, S. C., Eccles, J. D., Faulkner, D. R., et al. (2012). Drilling reveals fluid control on architecture and rupture of the Alpine Fault, New Zealand. *Geology*, *40*(12), 1143–1146. https://doi.org/10.1130/G33614.1

Tagami, T. (2005). Zircon fission-track thermochronology and applications to fault studies. *Reviews in Mineralogy and Geochemistry*, *58*(1), 95–122. https://doi.org/10.2138/rmg.2005.58.4

Tippett, J. M., & Kamp, P. J. J. (1993). Fission track analysis of the Late Cenozoic vertical kinematics of continental pacific crust, South Island, New Zealand. *Journal of Geophysical Research*, *98*(B9), 16,119–16,148. https://doi.org/10.1029/92JB02115

Townend, J., Sutherland, R., Toy, V. G., Doan, M. L., Célérier, B., Massiot, C., et al. (2017). Petrophysical, geochemical, and hydrological evidence for extensive fracture-mediated fluid and heat transport in the Alpine Fault's hanging-wall damage zone. *Geochemistry, Geophysics, Geosystems*, *18*, 4709–4732. https://doi.org/10.1002/2017GC007202

Townend, J., & Zoback, M. D. (2001). Implications of earthquake focal mechanisms for the frictional strength of the San Andreas fault system. *Geological Society, London, Special Publications*, *186*(1), 13–21. https://doi.org/10.1144/GSL.SP.2001.186.01.02

Townend, J., & Zoback, M. D. (2004). Regional tectonic stress near the San Andreas fault in central and southern California. *Geophysical Research Letters*, *31*, L15S11. https://doi.org/10.1029/2003GL018918

Toy, V. G., Craw, D., Cooper, A. F., & Norris, R. J. (2010). Thermal regime in the central Alpine Fault zone, New Zealand: Constraints from microstructures, biotite chemistry and fluid inclusion data. *Tectonophysics*, *485*(1-4), 178–192. https://doi.org/10.1016/j.tecto.2009 12.013

Toy, V. G., Prior, D. J., & Norris, R. J. (2008). Quartz fabrics in the Alpine Fault mylonites: Influence of pre-existing preferred orientations on fabric development during progressive uplift. *Journal of Structural Geology*, *30*(5), 602–621. https://doi.org/10.1016/j.jsg.2008.01.001

Upton, P., Craw, D., Caldwell, T. G., Koons, P. O., James, Z., Wannamaker, P. E., et al. (2003). Upper crustal fluid flow in the outboard region of the Southern Alps, New Zealand. *Geofluids*, *3*(1), 1–12. https://doi.org/10.1046/j.1468-8123.2003.00046.x

Upton, P., Koons, P. O., & Chamberlain, C. P. (1995). Penetration of deformation driven meteoric water into ductile rocks: Isotopic and model observations from the Southern Alps, New Zealand. *New Zealand Journal of Geology and Geophysics*, *38*(4), 535–543. https://doi.org/10.1080/00288306.1995.9514680

Upton, P., & Sutherland, R. (2014). High permeability and low temperature correlates with proximity to brittle failure within mountains at an active tectonic boundary, Manapouri tunnel, Fiordland, New Zealand. *Earth and Planetary Science Letters*, *389*, 176–187. https://doi.org/10.1016/j.epsl.2013.12.032

Vry, J. K., Baker, J., Maas, R., Little, T. A., Grapes, R., & Dixon, M. (2004). Zoned (Cretaceous and Cenozoic) garnet and the timing of high grade metamorphism, Southern Alps, New Zealand. *Journal of Metamorphic Geology*, *22*(3), 137–157. https://doi.org/10.1111/j.1525-1314.2004.00504.x

Vry, J. K., Powell, R., Golden, K. M., & Petersen, K. (2010). The role of exhumation in metamorphic dehydration and fluid production. *Nature Geoscience*, *3*(1), 31–35. https://doi.org/10.1038/ngeo699

Vry, J. K., Powell, R., & Williams, J. (2008). Establishing the P-T path for Alpine Schist, Southern Alps near Hokitika, New Zealand. *Journal of Metamorphic Geology*, *26*(1), 81–97. https://doi.org/10.1111/j.1525-1314.2007.00746.x

Walcott, R. I. (1998). Modes of oblique compression: Late Cenozoic tectonics of the south island of New Zealand. *Reviews of Geophysics*, *36*(1), 1. https://doi.org/10.1029/97RG03084

Wallace, L. M., Beavan, J., McCaffrey, R., Berryman, K., & Denys, P. (2007). Balancing the plate motion budget in the South Island, New Zealand using GPS, geological and seismological data. *Geophysical Journal International*, *168*(1), 332–352. https://doi.org/10.1111/j.1365-246X.2006.03183.x

Wannamaker, P. E., Caldwell, T. G, Doerner, W. M., & Jiracek, G. R. (2004). Fault zone fluids and seismicity in compressional and extensional environments inferred from electrical conductivity: The New Zealand Southern Alps and U. S. Great Basin. *Earth, Planets and Space*, *56*(12), 1171–1176. https://doi.org/10.1186/BF03353336

Wannamaker, P. E., Caldwell, T. G., Jiracek, G. R., Maris, V., Hill, G. J., Ogawa, Y., et al. (2009). Fluid and deformation regime of an advancing subduction system at Marlborough, New Zealand. *Nature*, *460*(7256), 733–736. https://doi.org/10.1038/nature08204

Wannamaker, P. E., Jiracek, G. R., Stodt, J. A., Caldwell, T. G., Gonzalez, V. M., McKnight, J. D., & Porter, A. D. (2002). Fluid generation and pathways beneath an active compressional orogen, the New Zealand Southern Alps, inferred from magnetotelluric data. *Journal of Geophysical Research*, *107*(B6), ETG 6–1-ETG 6-20. https://doi.org/10.1029/2001JB000186

Warren-Smith, E., Lamb, S., Seward, D., Smith, E., Herman, F., & Stern, T. (2016). Thermochronological evidence of a low-angle, mid-crustal detachment plane beneath the central South Island, New Zealand. *Geochemistry Geophysics Geosystems*, *17*, 4212–4235. https://doi.org/10.1002/2016GC006402

Wellman, H. W. (1979). An uplift map for the South Island of New Zealand, and a model for uplift of the Southern Alps, in The Origin of the Southern Alps. *Royal Society of New Zealand Bulletin*, *18*, 13–20.

Wellman, H. W., & Willet, R. (1942). The geology of the West Coast from Abut Head to Milford Sound—Part 1. Royal Society of New Zealand.

Wessel, P., Smith, W. H. F., Scharroo, R., Luis, J., & Wobbe, F. (2013). Generic mapping tools: Improved version released. *Eos, Transactions American Geophysical Union*, *94*(45), 409. https://doi.org/10.1002/2013EO450001

Zoback, M. D., & Townend, J. (2001). Implications of hydrostatic pore pressures and high crustal strength for the deformation of intraplate lithosphere. *Tectonophysics*, *336*(1-4), 19–30. https://doi.org/10.1016/S0040-1951(01)00091-9

Zoback, M. D., Townend, J., & Grollimund, B. (2002). Steady-state failure equilibrium and deformation of intraplate lithosphere. *International Geology Review*, *44*(5), 383–401. https://doi.org/10.2747/0020-6814.44.5.383